

Waves in Jupiter's atmosphere observed by the Cassini ISS and CIRS instruments

Liming Li^{a,*}, Andrew P. Ingersoll^a, Ashwin R. Vasavada^b, Amy A. Simon-Miller^c,
Richard K. Achterberg^d, Shawn P. Ewald^a, Ulyana A. Dyudina^a, Carolyn C. Porco^e,
Robert A. West^f, F. Michael Flasar^c

^a Division of Geological and Planetary Sciences, California Institute of Technology, Mail Stop 150-21, Pasadena, CA 91125, USA

^b Jet Propulsion Laboratory, California Institute of Technology, M/S 183-501, Pasadena, CA, USA

^c NASA/Goddard Space Flight Center, Code 693, Greenbelt, MD, USA

^d Science Systems and Applications, Inc., 5900 Princess Garden Parkway, Suite 300, Lanham, MD, USA

^e CICLOPS/Space Science Institute, 4750 Walnut Street, Ste 205, Boulder, CO, USA

^f Jet Propulsion Laboratory, California Institute of Technology, M/S 169-237, Pasadena, CA, USA

Received 23 March 2006; revised 18 July 2006

Available online 20 October 2006

Abstract

The Cassini Imaging Science Subsystem (ISS) and Composite Infrared Spectrometer (CIRS) reported a North Equatorial Belt (NEB) wave in Jupiter's atmosphere from optical images [Porco, C.C., and 23 colleagues, 2003. *Science* 299, 1541–1547] and thermal maps [Flasar, F.M., and 39 colleagues, 2004. *Nature* 427, 132–135], respectively. The connection between the two waves remained uncertain because the two observations were not simultaneous. Here we report on simultaneous ISS images and CIRS thermal maps that confirm that the NEB wave shown in the ISS ultraviolet (UV1) and strong methane band (MT3) images is correlated with the thermal wave in the CIRS temperature maps, with low temperatures in the CIRS maps (upwelling) corresponding to dark regions in the UV1 images (UV-absorbing particles) and bright regions in the MT3 images (high clouds and haze). The long period of the NEB wave suggests that it is a planetary (Rossby) wave. The combined observations from the ISS and CIRS are utilized to discuss the vertical and meridional propagation of the NEB wave, which offers a possible explanation for why the NEB wave is confined to specific latitudes and altitudes. Further, the ISS UV1 images reveal a circumpolar wave centered at 48.5° S (planetocentric) and probably located in the stratosphere, as suggested by the ISS and CIRS observations. The simultaneous comparison between the ISS and CIRS also implies that the large dark oval in the polar stratosphere of Jupiter discovered in the ISS UV1 images [Porco, C.C., and 23 colleagues, 2003. *Science* 299, 1541–1547] is the same feature as the warm regions at high northern latitudes in the CIRS 1-mbar temperature maps [Flasar, F.M., and 39 colleagues, 2004. *Nature* 427, 132–135]. This comparison supports a previous suggestion that the dark oval in the ISS UV1 images is linked to auroral precipitation and heating [Porco, C.C., and 23 colleagues, 2003. *Science* 299, 1541–1547].

© 2006 Elsevier Inc. All rights reserved.

Keywords: Atmospheres; dynamics; Jupiter; atmosphere; Planetary dynamics

1. Introduction

Atmospheric waves can serve as probes of atmospheric internal structures in the same way that seismic waves probe the internal structure of Earth (Flasar and Gierasch, 1986;

Bosak and Ingersoll, 2002). Also, waves are important for transporting momentum, energy, molecules, and particles between different latitudes and altitudes. Their presence provides information about the forces that drive them. Among the giant planets, waves are discovered to be ubiquitous in the atmospheres from thermal fields and optical images (Magalhaes et al., 1989; Orton et al., 1991, 1994; Deming et al., 1989, 1997; Achterberg and Flasar, 1996; Godfrey, 1988; Sanchez-Lavega et al., 1998). For Jupiter, optical images have revealed wave

* Corresponding author.

E-mail address: liming@gps.caltech.edu (L. Li).

patterns over a large range of spatial scales. Planetary waves with horizontal wavelength longer than 10,000 km were reported at high latitudes in Jupiter's stratosphere by the optical imaging system on Hubble Space Telescope (HST) (Sanchez-Lavega et al., 1998). At the same time, gravity waves with horizontal wavelength around 300 km were discovered in the planet's equatorial atmosphere in Voyager images (Flasar and Gierasch, 1986). Jupiter's horizontal thermal maps (Orton et al., 1991, 1994; Deming et al., 1997) and vertical temperature structure (French and Gierasch, 1974; Young et al., 2005) also revealed the large-scale planetary waves and meso-scale gravity waves. The equatorial 5 μ m hot spots, which allow 5 μ m thermal emission from deeper atmospheric level to escape due to their low cloud opacity, are observed in optical images (Allison, 1990), thermal maps (Ortiz et al., 1998; Orton et al., 1998), and numerical modeling (Showman and Dowling, 2000). The hot spots are interpreted as Jupiter's planetary waves in the above studies. For the other giant planets, waves are also discovered to be ubiquitous in the atmospheres from thermal fields and optical images (Godfrey, 1988; Hinson and Magalhaes, 1991, 1993; Achterberg and Flasar, 1996).

More recently, the Cassini ISS discovered an obvious longitudinal wave in Jupiter between 10 and 19° N latitude (planetocentric) from the ultraviolet (258 nm, UV1) and strong methane band (889 nm, MT3) images (Porco et al., 2003). Subsequently, the Cassini CIRS reported a thermal wave at the same latitude ranges from temperature maps (Flasar et al., 2004a, 2004b). Unfortunately, these two Cassini observations are not simultaneous so it was difficult to correlate the two waves and determine their relative phase. Some previous work (Magalhaes et al., 1989; Orton et al., 1994; Sanchez-Lavega et al., 1998) that tried to connect optical waves to the thermal waves suffered from the same problem. Fortunately, the Cassini ISS obtained multi-filter images of Jupiter (the ride-along data set) during the working time of the CIRS observations, which provide a good opportunity to study the correlation between the optical waves and thermal waves.

In this paper, we discuss the waves that were discovered by the ISS and CIRS. The wave between 10 and 19° N latitude (planetocentric) is a Rossby wave. By comparing the phase speed of the wave with the local wind speed, we are able to identify a region in latitude–altitude space where the wave can propagate. At the boundaries of the region the wave is either absorbed or reflected. These studies help identify the regions where the wave is generated. The simultaneous observations are also used to connect the large dark oval in the polar region discovered by the ISS UV1 images and the warm regions in the CIRS 1-mbar temperature maps.

The following section (Section 2) is a description of the data sets used in this paper. Our observations of waves are discussed in Section 3. Theoretical considerations are in Section 4. In Section 5, we summarize our discussion in the context of previous observations. Planetocentric latitudes, System III west longitude, and positive velocity in the eastward direction are used in this paper.

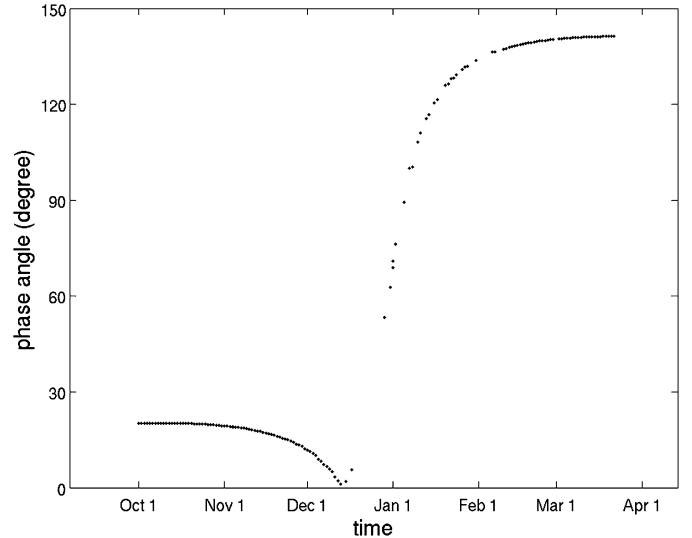


Fig. 1. Phase angle during the Cassini Jupiter flyby. The Jupiter flyby observation began in October 1 of 2000 and ended in March 22 of 2001. The phase angle decreased to minimal value (1°) in December 14 of 2000. Irregular blanks during the series of dots indicate no ISS or CIRS data in the corresponding time. The maximal period of missing data is from December 19 to 29 in 2000.

2. Description of data sets and processing

Our observations are made using three data sets: (1) the continuous ISS multi-filter images acquired over the 45-day period October 1 to November 14, 2000, (2) the ISS ride-along imaging data set, which was taken during the working time of the CIRS regular observations over the 10-day period January 1–10, 2001, and (3) temperature maps constructed from the CIRS data taken at the same time as the ride-along imaging data set, January 1–10, 2001. The spatial resolution of the Cassini ISS images at the equator ranges from ~ 500 km/pixel at the beginning of October in 2000 to ~ 100 km/pixel at the beginning of January in 2001. The CIRS thermal maps have spatial resolution of $\sim 1^\circ$ in the latitudinal and longitudinal directions, which corresponds to ~ 1000 km in the tropical regions of Jupiter.

The ISS acquired high-quality time-lapse images in different filters during its lengthy 6-month (October 1, 2000 to March 22, 2001) Jupiter flyby. The ISS multi-filter imaging data sets before the middle of December of 2000 are fairly regular in time and space, which covered the jovian global disk once per one or two jovian rotations, i.e., once every 10 or 20 h. The corresponding imaging strategy for these continuous images has been described elsewhere (Porco et al., 2003, 2004; Li et al., 2006). The phase angle between the spacecraft and Jupiter was 20° at the beginning of the flyby (October 1, 2000). The spacecraft began a month-long sweep through a large range of phase angles after its phase angle passed through zero on December 14 of 2000 (Fig. 1).

The image navigation, map projections, and radiometric calibration for these ride-along images are the same as used for the continuous ISS images (Porco et al., 2003, 2004; Li et al., 2006). For photometric calibration, the classical Minnaert correction (Minnaert, 1941) does not work well for these ride-along images because the phase angle is large and the physi-

cal properties of the atmosphere depend strongly on latitude. Therefore, we adopt a more empirical approach to define the Minnaert correction factor f . One divides by this number to get the normalized brightness at zero incidence and phase angles.

$$f = (\cos i)^{k(\phi)} (\cos e)^{l(\phi)}, \quad (1)$$

where i is the solar incidence angle and e is the emission angle. The indices $k(\phi)$ and $l(\phi)$ are set as functions of latitude ϕ . In order to maximize the feature contrast and minimize the seams, which appear when the neighboring images taken at different times are put together to make global maps, we make k and l change independently even though it violates the reciprocity principle (Minnaert, 1941). Further, in the MT3 and UV1 images, we subtracted the mean brightness of every line of pixels, corresponding to lines of constant latitude in the map-projected images, to enhance the contrast of the small-scale features and reveal some features covered by the equatorial haze.

The CIRS team produced temperature maps with high vertical and horizontal resolution (Flasar et al., 2004a, 2004b). Some CIRS thermal maps at specific pressure-levels (400-, 243-, 4-, and 1-mbar) at different times (January 1, 5, and 10, 2001) are utilized to make a simultaneous comparison with the ISS ride-along images in this paper.

3. Observations and analysis

3.1. Waves in the Cassini ISS multi-filter images

Fig. 2 shows an example of cylindrical-projected global maps in different filters constructed from the continuous ISS multi-filter image set. The ISS continuous images were taken at intervals of 40 s for the three filters (UV1, MT3 and CB3), which makes the constructed global maps in the three filters shown in Fig. 2 virtually simultaneous. The mean value of brightness in every constant-latitude line in the MT3 and UV1 images is removed so that the feature contrast covered by the equatorial haze in MT3 and UV1 can be seen. In the UV1 (258 nm) and MT3 (889 nm) global maps, the most conspicuous wave is observed between 10 and 19° N latitudes with a clear anti-correlation between the UV1 and MT3 maps. The anti-correlation implies that this North Equatorial Belt (NEB) wave is composed of UV-absorbing small particles mixed with the high-altitude scattering haze, both of which absorb in the UV1 and scatter in the MT3. Also, the gases in the atmosphere absorb in the MT and scatter in the UV. The number of wavelengths in the planetary circumference for the NEB wave is 12–13, which corresponds to a wavelength of 34,000–37,000 km at 14.5° N. The quasi-periodic bright areas around 60, 120, 180, 240, and 300° W in the top and bottom boundaries of the MT3 global map (panel B) come from incomplete removal of limb darkening.

The so-called 5 μ m hot spots revealed by the 5 μ m thermal measurements are also observed by the Cassini ISS images at the visible bands and methane-absorption bands. The CB3 global map in Fig. 2 displays these hot spots, which are dark patches located in Jupiter's bright equatorial band. These hot

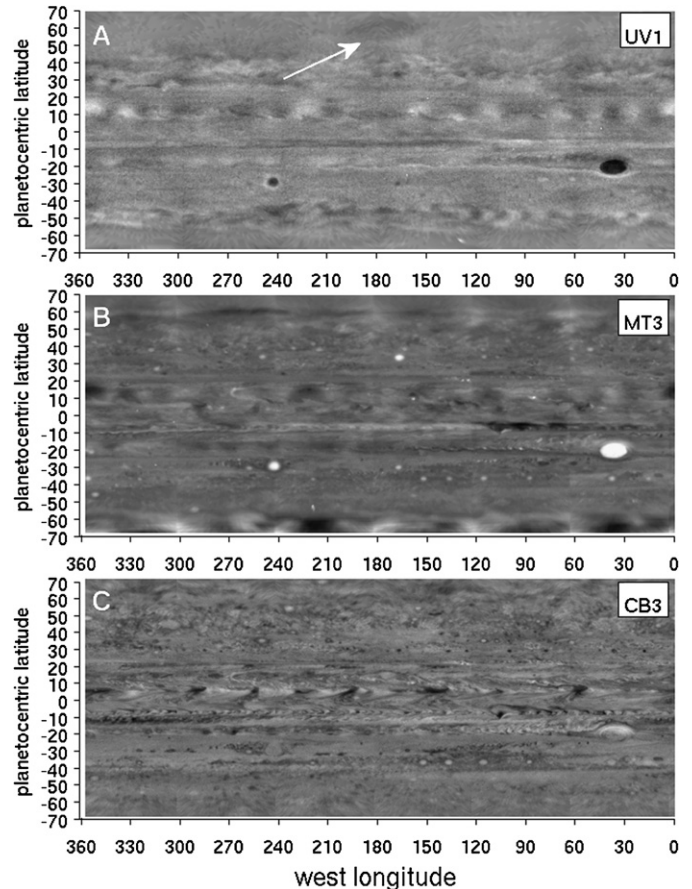


Fig. 2. Cylindrical-projected ISS global maps in multi-filter. The ISS images used in the three global maps were taken on 1 November 2000 with intervals of 40 s between the three filters (UV1, MT3, and CB3). The mean brightness of every line of pixels in the MT3 and UV1 images is removed so that the feature contrast covered by the equatorial haze in MT3 and UV1 can be seen. Note that the quasi-periodic bright areas around 60, 120, 180, 240, and 300° W in the top and bottom boundaries of the MT3 global map are not real features. They mainly come from incomplete photometric calibration due to high incidence and emission angles in polar region.

spots are different from the NEB wave in the UV1 and MT3 global maps: First, they are located at a different latitude, and second, they have a different longitudinal pattern than the NEB wave. The MT3 global map of Fig. 2 shows both the NEB wave centered at 14.5° N and these hot spots centered at 5° N, which confirms that they are different phenomena. Previous studies show that the number of hot spots encircling the planet changed from 13 during the Voyager 1 encounter to 11 during the Voyager 2 encounter (Smith et al., 1979a, 1979b). The number decreased to 8–10 at the time of Cassini, as seen in the CB3 global map of Fig. 2.

Fig. 2 shows that the NEB wave cannot be seen in the continuum band CB3 global map centered at 938 nm, even though that band is close in wavelength to the MT3 band at 889 nm. The NEB wave pattern shows clearly only in the UV1 and MT3 among the 9 filters of the Cassini ISS (Fig. 3). Some features seen in the other 7 filters may be related to features of the wave that are seen in the UV1 and MT3 filters (Porco et al., 2003), but the correlation is weak. We suggest two possibilities: One is that the NEB wave exists at the pressure levels

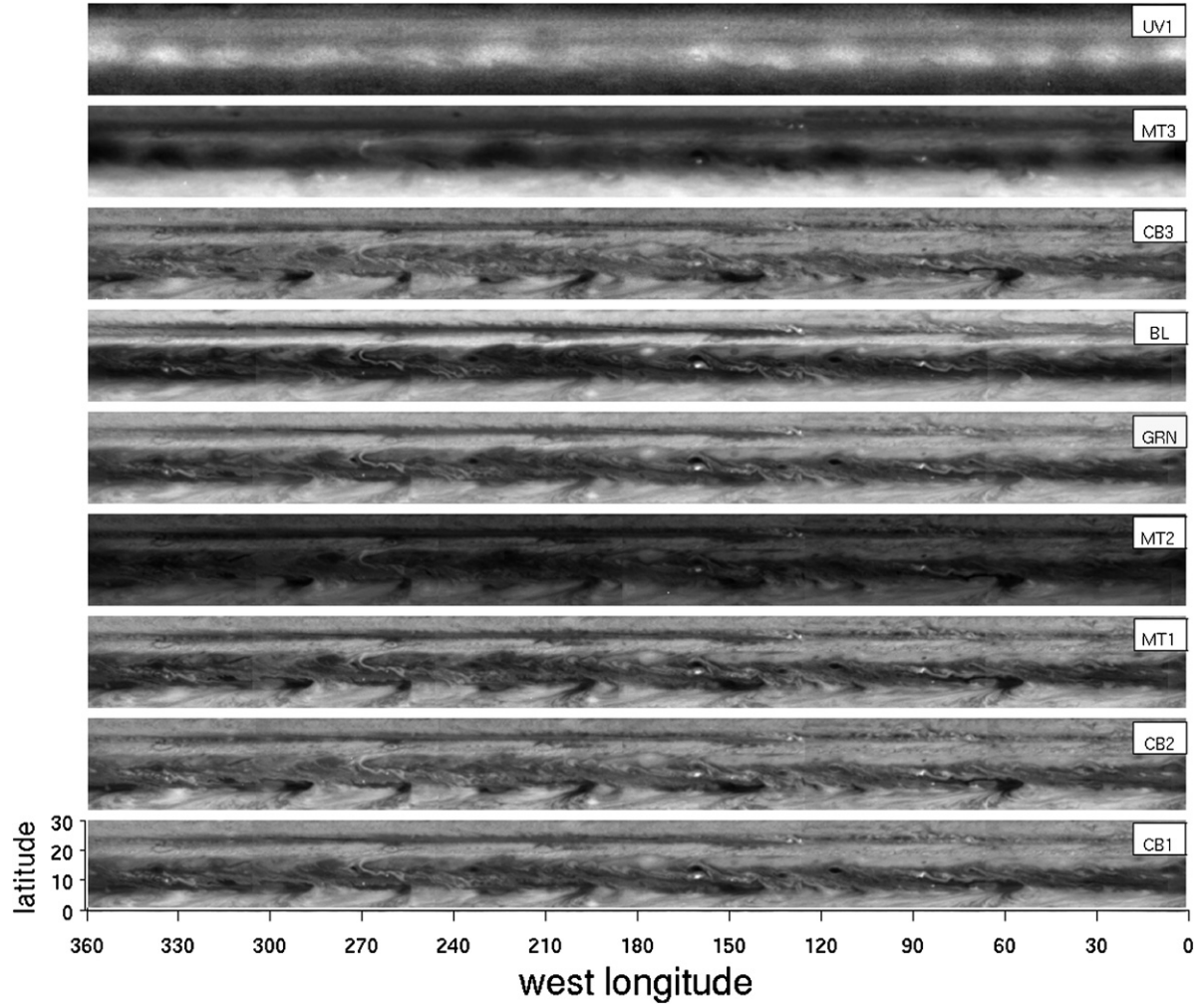


Fig. 3. Cylindrical-projected ISS maps of the NEB waves in nine filters. The images were taken on 1 November 2000 with intervals of 40 s, which makes them virtually simultaneous.

sampled by the 7 filters, but the mechanism to produce contrast from the wave activity is weak there. The other is that the NEB wave does not exist at the altitudes sampled by the 7 filters. The effective pressure-levels (optical depth $\tau = 1$ in the absence of cloud opacity) in the UV1 and MT3 filters are 350- and 600-mbar, respectively (West et al., 2004; Li et al., 2006). These pressure-levels are higher in altitude than the effective pressure-levels in the other 7 filters. The cloud features seen in the continuum band images are estimated to be at a pressure-level ~ 0.7 bar (Banfield et al., 1998), so the second possibility would imply that the bottom of the NEB wave is above the 0.7 bar surface.

A circumpolar wave system centered at 48.5° S is seen in the UV1 global map of Fig. 2, but not in the other 8 filters of the ISS images. The polar-projected map of panel A of Fig. 2 is displayed in Fig. 4, which clearly shows that the wave encircles the polar region in the southern hemisphere. The stratospheric haze on Jupiter has significant opacity at UV wavelengths at high latitudes (Tomasko et al., 1986; West, 1988; Rages et al., 1999; West et al., 2004), which is probably due to auroral destruction of methane with subsequent ion and neutral chemistry (Hord et al., 1979; Pryor and Hord,

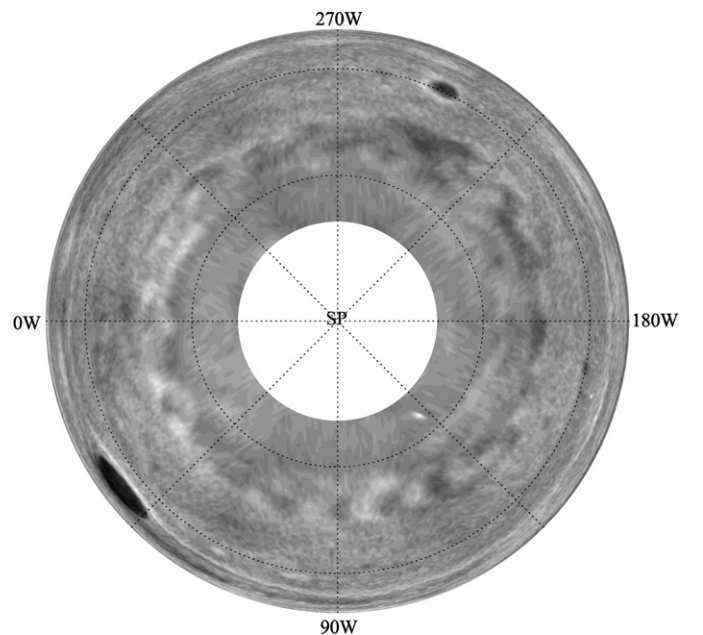


Fig. 4. Polar-projected map of southern hemisphere of the UV1 global map of Fig. 2. The 30 and 60° N latitude circles are shown in the figure.

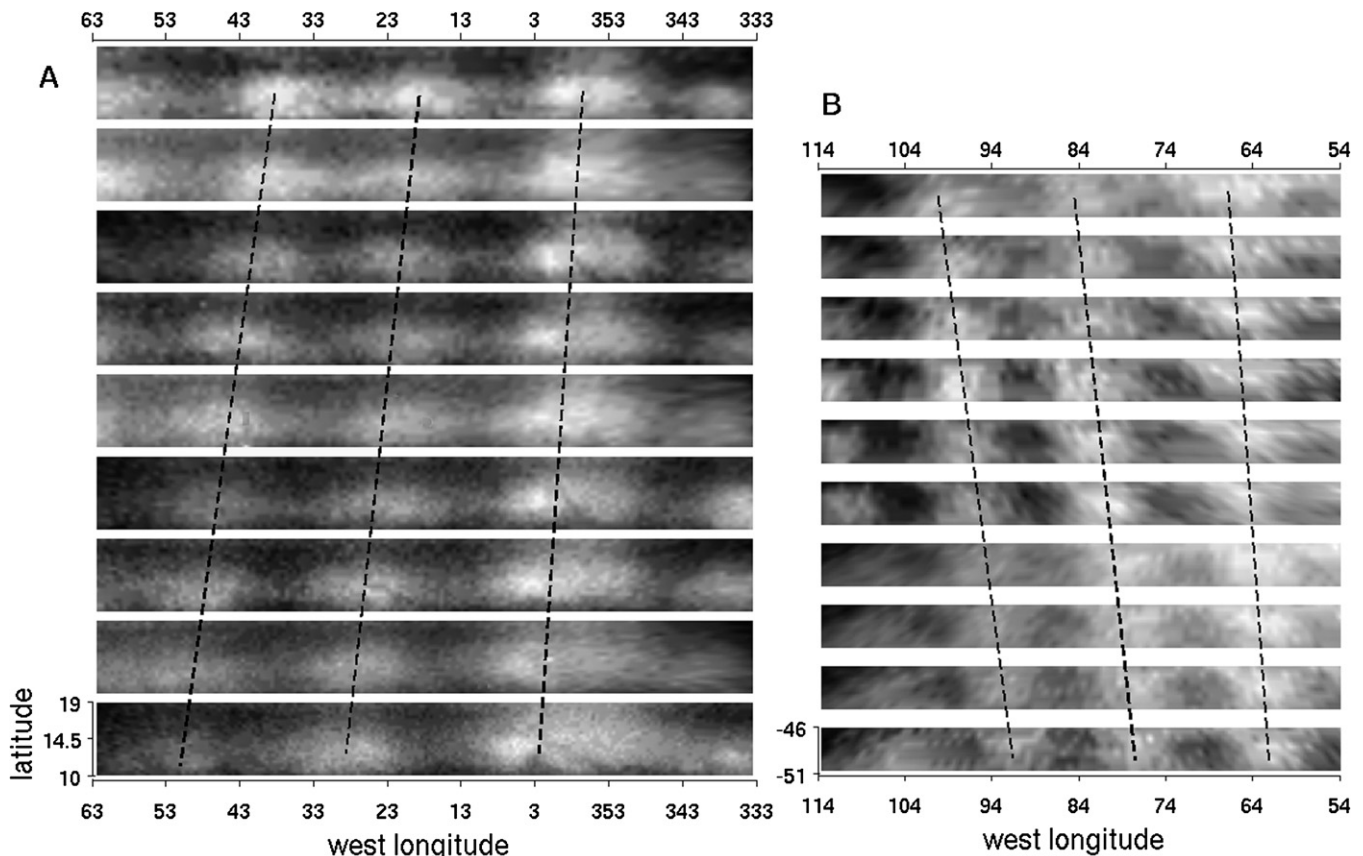


Fig. 5. Time series of the NEB wave and the circumpolar wave in the UV1 filter. (A) Time series of the NEB wave with the time separation 5 days, which began on 2 October 2000 and ended on 10 November 2000. (B) Time series of the circumpolar wave with the time separation 1.7 days, which began on 28 October 2000 and ended on 12 November 2000. The dashed lines indicate the movements of the three crests.

1991). In addition, estimates of the pressure levels of high-latitude features in ultraviolet images (Banfield et al., 1996; Vincent et al., 2000) suggest that, at high latitudes, the ultraviolet filter mainly senses the stratosphere. The above discussion combined with the fact that the circumpolar wave only shows in the UV1 images suggests that it is probably located in the stratosphere. The number of wavelengths in the corresponding planetary circumference for the circumpolar wave is estimated to be 18–20, which corresponds to a wavelength of 15,000–17,000 km at 48.5° S.

Many circumpolar waves were observed in mid-latitudes of the northern hemisphere in the UV1 global map of Fig. 2 (Porco et al., 2003). These circumpolar waves in the northern hemisphere do not show in the other 8 filters of the Cassini ISS images either, which similarly suggests that these waves are located in the stratosphere. The chaotic appearance of these waves makes it difficult to measure their features.

The NEB wave and circumpolar mid-latitude wave approximately kept their wave-numbers during the period of the continuous ISS images set over 45 days (October 1 to November 15, 2000) with small changes in the brightness and shapes of wave crests and troughs. Phase velocities relative to System III are measured by choosing clear parts of the two waves and tracking the motions of the crests. Fig. 5 shows the time series of the clear parts for the two waves in the UV1 filter. Panel A is for the NEB wave with the time separation 5 days, and panel B is

for the circumpolar wave with the time separation 1.7 days. The figure shows that the NEB wave steadily moves to the west with a drift of 11° of longitude during a 40-day period and the circumpolar wave steadily moves to the east with a drift of 8.5° of longitude during a 15-day period. The average phase velocities are calculated by averaging the movements of the three crests in the two waves, which are displayed in Fig. 6 as red dots with error-bars (panel A is for the NEB wave and panel B is for the circumpolar wave). The error-bars are estimated by the standard deviation of the velocities of the three crests. The two average phase velocities relative to System III are $c_x = -3.9 \text{ m s}^{-1}$ for the NEB wave and $c_x = 4.2 \text{ m s}^{-1}$ for the circumpolar wave. The wave periods relative to System III for the two waves are estimated as ~ 100 days for the NEB wave and ~ 50 days for the circumpolar wave by taking account of the corresponding zonal wavelength and phase velocity.

Fig. 6 shows the ambient flows at the pressure levels of the UV1 filter (red line) and CB2 filter (green line) within the latitude ranges of the two waves. The velocities of the ambient flows in the UV1 filter come by tracking the small features unique to the UV1 images in the continuous ISS multi-filter image sets acquired over a 45-day period (Li et al., 2006). The small features are distinct from the wave itself, which has a larger scale. The comparison with the CIRS thermal wind suggests that the ambient flows from UV1 images are located at a pressure level of 0.5 bar (Li et al., 2006). The UV1 ambi-

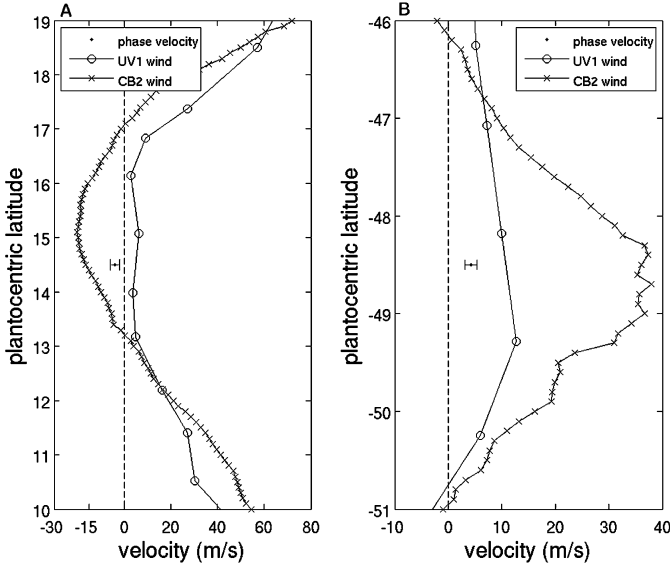


Fig. 6. Velocities of the ambient flows within the latitude ranges of the NEB wave and the circumpolar wave in the UV1 and CB2 filters and average phase velocities of the two waves. (A) The NEB wave. (B) The circumpolar wave. The red solid lines are the velocities of the ambient flows in the UV1 filter coming from previous measurements by tracking the small features unique to the UV1 (Li et al., 2006). The green solid lines are the velocities of the ambient flows in the CB2 filter coming from an automatic-correlated measurement based on the time-lapse CB2 images in the Cassini ISS data sets (Porco et al., 2003). The red dots with error-bars are the mean phase velocities of the two waves by averaging the velocities of the three crests in (A) and (B) of Fig. 2. The error-bars are estimated by the standard deviation of the velocities of the three crests.

ent flows outside equatorial regions are probably located at a higher altitude than 0.5 bar due to the increase of stratospheric opacity at high latitudes (Tomasko et al., 1986; West, 1988; Rages et al., 1999; West et al., 2004). The green line comes from an automatic-correlation measurement based on the time-lapse CB2 images in the ISS data set (Porco et al., 2003), which represents an ambient flow at the pressure level ~ 0.7 bar (Banfield et al., 1998). The phase velocities of the waves and the corresponding UV1 ambient flows come from the same ISS UV1 image set over a 45-day period, which implies that the waves and the UV1 ambient flows are around the same pressure-level. Fig. 6 shows that the two waves propagate westward relative to the UV1 flow at its altitude, although they propagate eastward relative to the CB2 flow at its altitude. Since the CB2 flow is at a lower altitude than the wave, this difference has important implications for wave propagation, which will be discussed in Sections 4.2 and 4.3.

3.2. The NEB wave in ISS and CIRS images

The MT3 filter images during the ride-along imaging period (Jan. 1 to Jan. 10, 2001) are spaced in a regular pattern compared to the UV1 filter images, so we can make MT3 global maps during the period. Fig. 7 shows a simultaneous comparison between an ISS MT3 global map and the CIRS global temperature field. Panel A is the CIRS 400-mbar global temperature field on 1 January 2001. The CIRS global temperature maps discussed in this paper are the actual retrieved temperatures at specific pressure levels (Flasar et al., 2004b). Panel B is

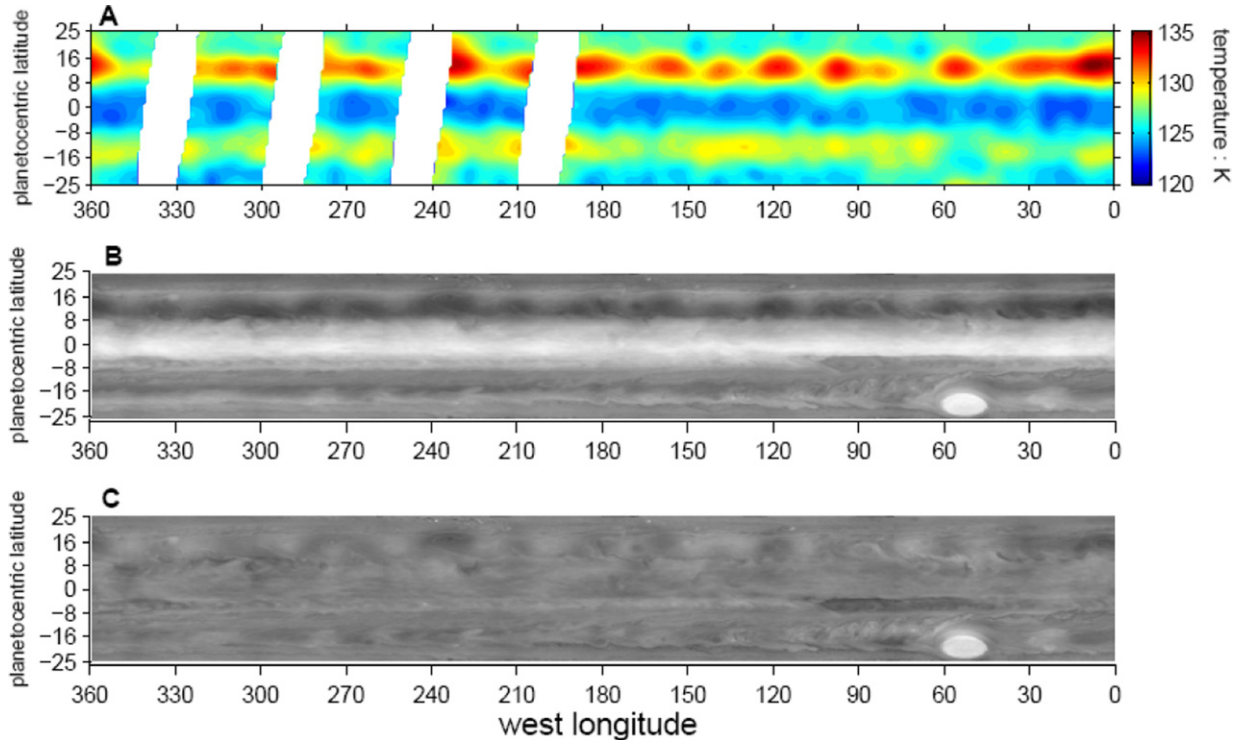


Fig. 7. Simultaneous comparison between the CIRS global temperature map and the ISS MT3 global map in the equatorial regions. (A) The CIRS global temperature map at pressure level 400 mbar on 1 January 2001. White areas in (A) indicate gaps in the CIRS data coverage. (B) The ISS MT3 global map at the same time with (A). (C) Same with (B) except for removing mean value of every constant-latitude line to increase the feature contrast.

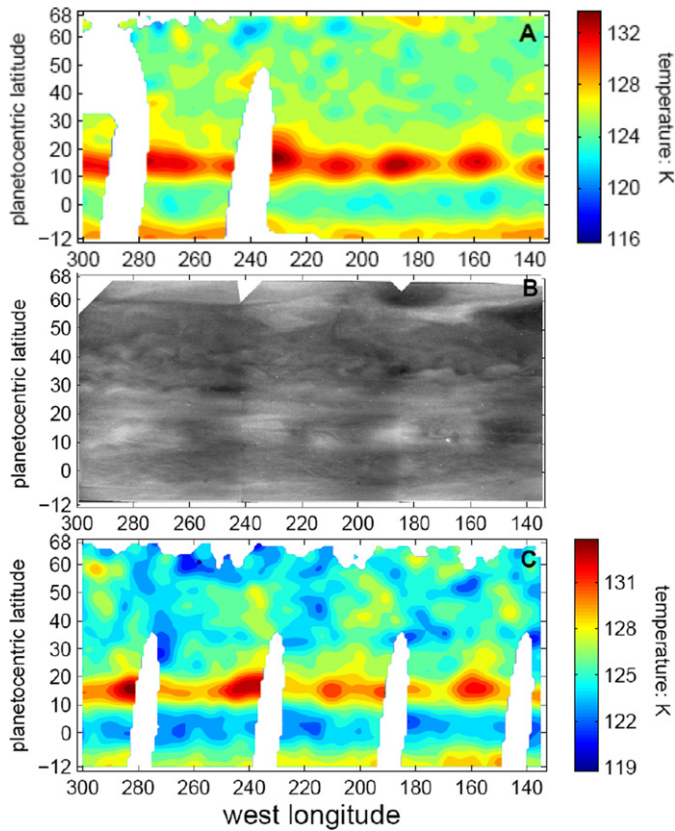


Fig. 8. Near-simultaneous comparison for the NEB wave between the CIRS temperature maps and the ISS UV1 map. (A) The CIRS 400-mbar temperature map between longitude 135 to 300° W and latitude 12° S to 69° N on 5 January 2001. (B) The ISS UV1 map in the same location (longitude 135 to 300° W and latitude 12° S to 69° N) on 7 January 2001. The mean value of every constant-latitude line in the UV1 map is removed to increase the feature contrast. (C) Same with (A) except for a different time (10 January 2001). White areas in (A) and (C) and in the boundaries of (B) indicate gaps in the data coverage.

the ISS MT3 global map at the same time. Panel C is the same as panel B except the mean value of every constant-latitude line was removed to increase the feature contrast. The simultaneous comparison displays a clear negative correlation between the ISS MT3 bright regions and the CIRS high temperatures for the NEB wave. It also suggests that the bright regions of the NEB wave in UV1 images are positively correlated with high

temperatures in the CIRS maps because of the anti-correlation between the UV1 and MT3 for the NEB wave. The following near-simultaneous comparison between the ISS UV1 and CIRS (Fig. 8) confirms this point.

During the ride-along imaging period, the UV filter images are irregular in time and space and relatively scarce compared to the MT3 filter images. Therefore, we cannot make a whole UV1 global map during the period. Panel B in Fig. 8 shows a UV1 map from longitude 135 to 300° W and latitude 12° S to 69° N on 7 January 2001. Likewise, the mean value of every constant-latitude line is removed to increase the feature contrast. We do not have the CIRS temperature map at exactly the same time, so the CIRS 400-mbar temperature maps in January 5 (panel A) and January 10 (panel C) are used for the comparison in Fig. 8. All three CIRS 400-mbar thermal maps (January 1, 5 and 10, 2001) are put together (Fig. 9) to measure the movement of the NEB thermal wave. Fig. 9 shows that most of these thermal features move to the west with a longitude displacement $\sim 2^\circ$ during the 10-day period, which is roughly consistent with the measurement by the continuous UV1 images (11° during the 40-day period). The 2° longitude displacement during the 10-day period is only a small fraction of the wavelength of the NEB wave, so the comparison between the ISS UV1 image and the CIRS maps in Fig. 8 can be regarded as near-simultaneous observations. Fig. 8 displays a clear positive correlation for the NEB wave between the bright regions in the ISS UV1 map and the high temperatures in the CIRS thermal maps. In summary, the simultaneous comparison between the MT3 global map and the CIRS temperature field and the near-simultaneous comparison between the UV1 map and the CIRS thermal maps both suggest that the NEB wave appearing in the ISS images and the CIRS temperature field are parts of the same phenomenon. The low temperatures in the CIRS maps imply upward displacement of low-entropy air from below. The upward displacement is probably associated with these UV-absorbing small particles either by bringing them up from below or forming them during the process of upward displacement.

Fig. 10 shows CIRS thermal maps at four pressure levels—400, 243, 4, and 1 mbar. The NEB wave is apparent at 400 and 243 mbar but not at the 4 or 1 mbar levels. The simplest interpretation is that the wave does not exist at the higher levels.

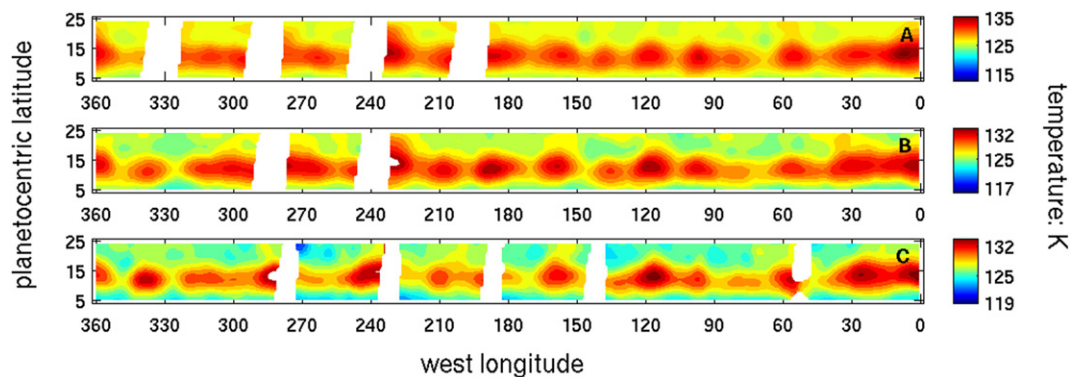


Fig. 9. Time series of the NEB wave in the CIRS 400-mbar thermal maps. Panels (A), (B), and (C) are the CIRS 400-mbar thermal maps on 1, 5 and 10, January 2001, respectively. White areas in (A), (B) and (C) indicate gaps in the data coverage.

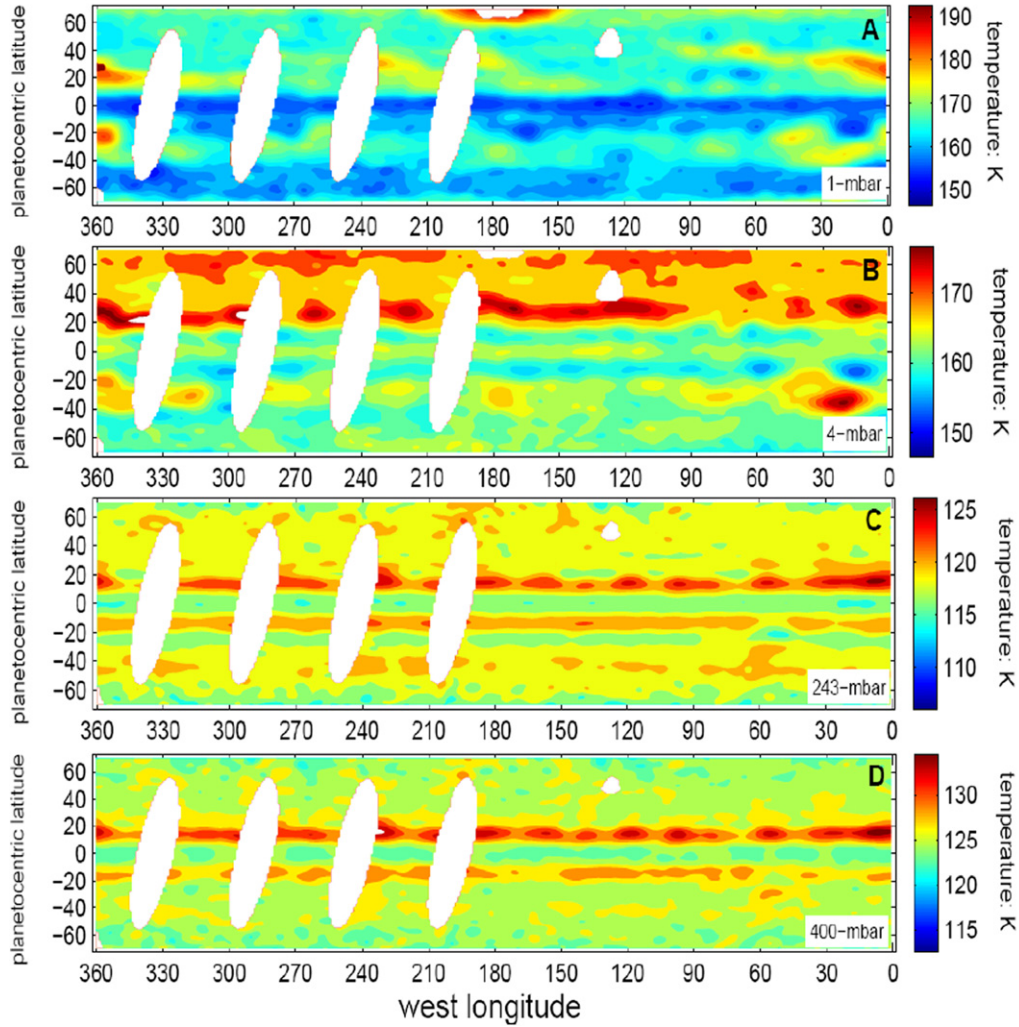


Fig. 10. Simultaneous CIRS thermal maps at different pressure-levels. (A) The CIRS 1-mbar global temperature map on 1 January 2001. (B), (C), and (D) are same as (A) except for different pressure-levels (4-, 243-, and 400-mbar, respectively). White areas in these temperature maps indicate gaps in the CIRS data coverage.

Ground-based observation (Orton et al., 1994) revealed waves in the temperature field (thermal waves) between 1980 and 1993, which are located around 13° N latitude and the 250-mbar pressure level with zonal wavelengths of order 40,000 to 70,000 km and phase velocity of -5.5 m s^{-1} relative to System III. Hubble Space Telescope (HST) wide field planetary camera 2 (WRPC2) observations taken between 1995 and 1996 in the visible wavelengths and methane bands (Simon-Miller et al., 2001) also showed a wave system with roughly the same wavelength and latitudes as the NEB wave in this paper. The similarity between the waves discovered by the previous observations and the NEB wave observed by Cassini during 2000–2001 suggests that the NEB wave is a recurring phenomenon or a long-lived system.

3.3. The circumpolar wave in ISS and CIRS images

No high-latitude UV1 images in the southern hemisphere of Jupiter are found from the ISS ride-along imaging data set during January 1–10, 2001, so we cannot connect the circumpolar wave centered at 48.5° S to the CIRS thermal maps directly.

However, these CIRS temperature maps at different pressure levels (400-, 243-, 4-, and 1-mbar) in January 1 of 2001, which is displayed in Fig. 10, do not show this wave pattern around 48.5° S. Therefore, the circumpolar wave centered at 48.5° S latitude probably exists in a pressure levels between 243- and 4-mbar if we assume that the circumpolar wave lived through the first week of January in 2001.

3.4. The 65° N oval in ISS and CIRS images

The ISS 2.5-month (October 1 to mid-December, 2000) UV1 movie displays a large dark oval centered at 65° N in Jupiter with the same size and shape as the Great Red Spot (Porco et al., 2003). Although this feature is not long-lived, a nearly identical feature had been seen in HST images taken in 1997 (West et al., 2004). The UV1 global map of Fig. 2 (panel A) shows a dark oval formed in the beginning of November in 2000 with position (65° N, 170° W), and is indicated by a white arrow. The dark oval does not show in the strong methane band (MT3) and the corresponding continuum band (CB3). This and the fact that the UV1 light cannot penetrate to the tro-

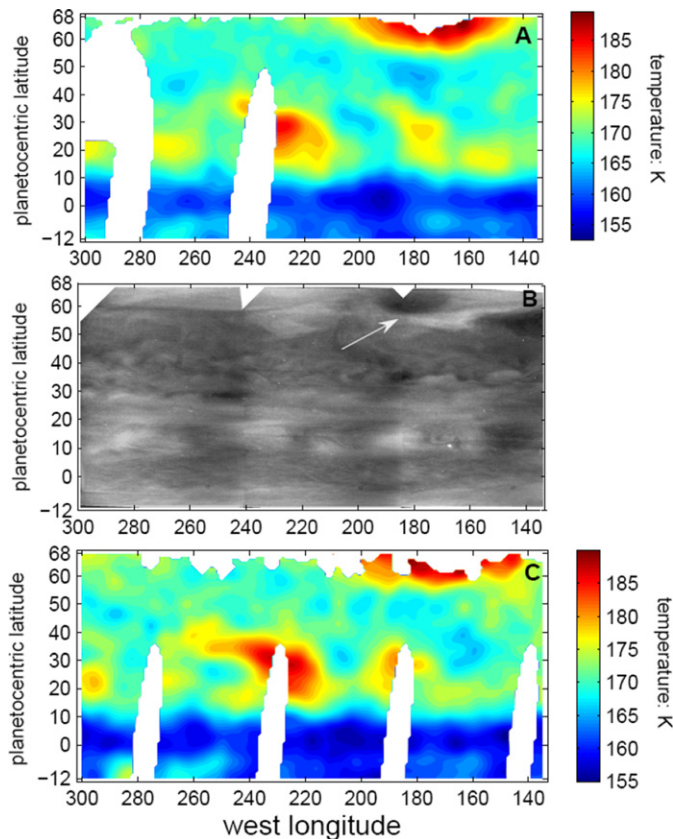


Fig. 11. Near-simultaneous comparison on the large oval feature between the CIRS temperature maps and the ISS UV1 map. This figure is same as Fig. 8 except that the CIRS temperature maps are in a high-altitude pressure-level (1-mbar). The dark oval in the ISS UV1 maps is indicated by a white arrow.

posphere in the polar region due to the intense stratospheric haze (Tomasko et al., 1986; West, 1988; Rages et al., 1999; West et al., 2004), suggest that the dark oval is located in the stratosphere (Porco et al., 2003). The oval formed and grew from early October to mid-November, then elongated and died at the end of the 2.5-month period (Porco et al., 2003). Other observations suggest that large oval formation in the polar region is a recurring phenomenon (West et al., 2004). Panel B of Fig. 11 shows a new dark oval indicated by a white arrow, which is centered at 65° N and 180° W and formed on 8 January 2001 after the old large oval died in the middle of December. The new dark oval implies that the polar oval is a recurring event. Flasar et al. (2004a, 2004b) also reported large warm regions in January of 2001 at the same latitude (65° N) in the CIRS 1-mbar temperature maps, but it is speculative to connect the CIRS warm regions to the UV1 dark oval in November of 2000 because the two observations are not simultaneous. Our UV1 maps in January 7 make it possible to study the correlation.

Fig. 11 shows a near-simultaneous comparison between the 1-mbar CIRS temperature maps and the ISS UV map. Panel B of Fig. 11 is the same as panel B of Fig. 8, which is the UV1 map on 7 January 2001. Panels A and C are the CIRS 1-mbar temperature maps in January 5 and 10, respectively. Fig. 11 suggests that the location and shape of the warm regions do not change much from January 5 to 10. The figure

also shows that the dark oval in the UV map has the same location (65° N, 180° W) and oval shape as the warm regions in the CIRS temperature maps. This comparison suggests that the dark oval in the UV1 images is connected to the high-latitude warm regions in the CIRS temperature maps. This relation is opposite to the NEB wave, where dark regions in UV1 images are connected to cold temperatures in the CIRS thermal maps. There the explanation was that the upward displacement of low-entropy air, corresponding to low temperatures in the CIRS maps, brings these small UV-absorbing particles from below or helps to form them. The correlation between the dark oval in the UV1 images and the warm regions in the CIRS thermal maps suggests that auroral processes play an important role in heating the air and forming the particles (Porco et al., 2003). Downward displacement of high-entropy air might bring these UV-absorbing particles down from above. The location of the new dark oval in January (65° N, 180° W) within the main auroral oval supports the connection between the dark oval and auroral process (Porco et al., 2003; Flasar et al., 2004a). In addition, the warm regions shown in the CIRS 1-mbar temperature maps do not show in the CIRS 4-mbar temperature maps (Fig. 11), which suggests the dark oval in the UV1 images is probably located above the 4-mbar pressure surface. This conclusion is consistent with the previous inference from limb darkening observations, which also implies that the dark oval is at 1-mbar or higher (West, 1988; West et al., 2004).

However, the warm regions in the CIRS temperature maps (panels A and C of Fig. 11) are larger than the dark oval in the UV1 map (panel B of Fig. 11). Likewise, Figs. 7 and 8 also show that the NEB wave in the CIRS temperature maps is larger than the NEB wave in the UV1 and MT3 images. We do not have an explanation why the size difference exists between brightness features in the ISS images and the thermal features in the CIRS temperature maps.

4. Theoretical considerations

4.1. Gravity waves versus planetary waves

The low frequency (period ~ 100 days) suggests that these are planetary waves—they cannot be gravity waves or acoustic waves. If the NEB wave were a gravity wave, its frequency relative to the zonal flow \bar{u} would be (Holton, 2004, p. 208)

$$(\nu - k\bar{u})^2 = f_0^2 + \frac{N^2 K_h^2}{m^2}, \quad (2)$$

where ν is frequency, k is zonal wave-number, \bar{u} is the ambient zonal wind, f_0 is the Coriolis parameter at the latitude of the NEB wave (14.5° N), N is the buoyancy (Brunt–Väisälä) frequency, K_h is the horizontal wave-number, and m is the vertical wave-number. The Coriolis parameter $f_0 = 9.1 \times 10^{-5} \text{ s}^{-1}$ at the latitude 14.5° N. The term $k\bar{u}$ is much smaller than the Coriolis parameter f_0 for the NEB wave with $k = 1.77 \times 10^{-7} \text{ m}^{-1}$ and $\bar{u} < 50 \text{ m s}^{-1}$ at the latitude 14.5° N. Therefore $|\nu| > |f_0|$, implying a period shorter than 0.8 days, but this is inconsistent

with the period of the NEB wave, which is ~ 100 days. Previous observations (French and Gierasch, 1974) also show that the period of jovian gravity waves in the upper atmosphere is less than 1 day. Therefore, we can rule out the gravity wave as the candidate of the NEB wave. The 48.5° S circumpolar wave can be ruled out as gravity wave for the same reason. Therefore, we think that the two waves (14.5° N wave and 48.5° S wave) are planetary waves.

4.2. Meridional trapping of the NEB wave

The NEB wave is observed between latitudes of 10° and 19° . We treat it as a planetary (Rossby) wave and ask if the wave is trapped within this band. With the data at hand, there are limitations to this analysis. Wave propagation and trapping depend on the zonal wind profile and static stability, and these are not precisely known at all the latitudes and altitudes of interest. Also, the vertical and horizontal structure of the wave is known at only a few latitudes and altitudes. Therefore a full-wave solution is not warranted, and we use the Wentzel–Kramer–Brillouin (WKB) approximation instead. Further, we use the WKB approximation beyond its range of validity, which is when the wavelength is much less than the scale of variation of the medium in which it propagates. However as stated by Morse and Feshbach (1953, p. 1105), even when this condition is not satisfied, the WKB method is often a convenient starting point for further analysis.

Consistent with this approximation, we assume that the NEB wave has solutions of the form $\exp[(z/2H) + i(kx - c_x kt + \int m dz)] \cos(\int l dy)$. Substituting this into the equation for small-amplitude quasi-geostrophic planetary waves on a β -plane (e.g., Salby, 1996, p. 463), we obtain the following dispersion relation for the square of the meridional wavenumber:

$$l^2 = \frac{\beta_e}{\bar{u} - c_x} - \frac{f^2}{N^2} \left(m^2 + \frac{1}{4H^2} \right) - k^2. \quad (3)$$

Quasi-geostrophic theory is valid here because the relative frequency $k(\bar{u} - c_x)$ is much smaller than f at the latitude of the NEB wave (14.5° N).

If l^2 is positive within a specific latitude range and negative outside that range, then the wave may be trapped within that range. Trapping therefore depends not only on the properties of the wave like m^2 , k^2 , and c_x , but also on the properties of the medium like β_e , \bar{u} , N^2 , H^2 , and f^2 . Here β_e is the meridional gradient of zonal-mean vorticity, and H is the scale height. Other variables have been defined in Eq. (2). In a zonal-mean flow $\bar{u}(y, z)$, β_e is defined by (Salby, 1996, p. 465)

$$\beta_e = \beta - \frac{\partial^2 \bar{u}}{\partial y^2} - \frac{1}{\bar{\rho}} \frac{\partial}{\partial z} \left(\bar{\rho} \frac{f_0^2}{N^2} \frac{\partial \bar{u}}{\partial z} \right) = \beta + \beta_y + \beta_z. \quad (4)$$

The meridional gradient of zonal-mean vorticity β_e is composed of three parts: The gradient of the planetary vorticity $\beta = \partial f / \partial y$, the vorticity gradient associated with the curvature of the ambient flows in the meridional direction $\beta_y = -\partial^2 \bar{u} / \partial y^2$, and the term associated with vertical shear of the ambient flows $\beta_z = -(1/\bar{\rho})(\partial/\partial z)[(\bar{\rho} f^2/N^2)(\partial \bar{u}/\partial z)]$. The vertical coordinate z in β_z is defined as $z = -H \ln(p/p_0)$ in the log-pressure

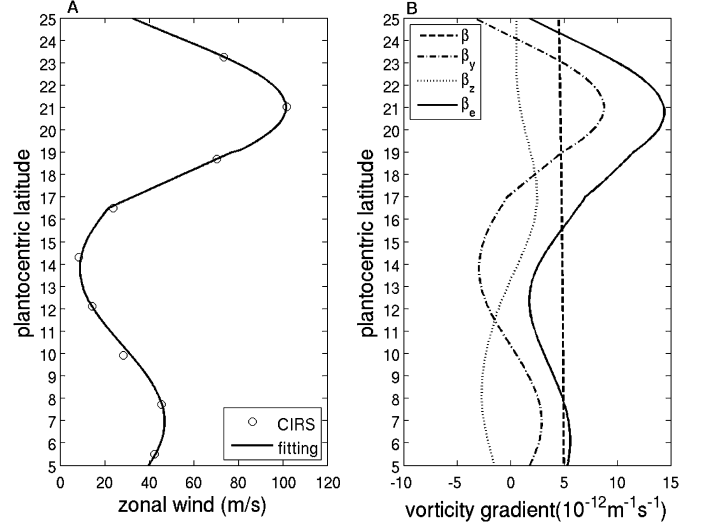


Fig. 12. CIRS 315-mbar zonal wind profile and meridional gradients of vorticity within the latitude range of the NEB wave. (A) The CIRS 315-mbar zonal wind profile around the latitude range of the NEB wave and a cosine function fit. The cosine function is set to have different amplitudes for the 21° N eastward jet and the 7.5° N westward jet. (B) The vorticity gradients β , β_y , β_z , and β_e at 315-mbar.

coordinates, where H is the reference scale height and p_0 is a reference pressure, e.g., one bar.

The estimation of β_e depends on the meridional and vertical structure of the zonal wind $\bar{u}(y, z)$, which we obtain from the CIRS data. We assume that the NEB wave is located around the 400- and 243-mbar levels based on the observations that the wave shows there but not at the 4- and 1-mbar levels (Fig. 10). We use the CIRS 315-mbar zonal winds, which are near the middle of the two pressure-levels (400- and 243-mbar). The first term β has the value $4.9 \times 10^{-12} \text{ s}^{-1} \text{ m}^{-1}$ at 14.5° N and changes smoothly with latitude (panel B of Fig. 12). We estimate β_y by fitting the CIRS 315-mbar zonal wind with two cosine functions and calculating β_y based on that function. Fig. 12 shows the result (panel A) and the corresponding β_y (panel B). Assuming that N^2 is constant and combining with the thermal wind equation, we can re-write the third term β_z of Eq. (4) in the form

$$\beta_z = \frac{gf}{TN^2} \left[\frac{\partial^2 T}{\partial z \partial y} - \left(\frac{1}{H} + \frac{1}{T} \frac{\partial T}{\partial z} \right) \frac{\partial T}{\partial y} \right]. \quad (5)$$

Therefore, the third term β_z can be estimated from the CIRS temperature fields with relatively higher spatial resolution ($\sim 1^\circ$ latitude) compared to the CIRS zonal winds fields ($\sim 2.2^\circ$ latitude). We approximate $\partial^2 T / \partial z \partial y$, $\partial T / \partial y$, and $\partial T / \partial z$ at 315-mbar by $(1/\Delta z)[(\partial T / \partial y)_{243} - (\partial T / \partial y)_{400}]$, $(1/2)[(\partial T / \partial y)_{243} + (\partial T / \partial y)_{400}]$, and $(1/\Delta z)(T_{243} - T_{400})$, respectively. The meridional gradients of temperature $(\partial T / \partial y)_{243}$ and $(\partial T / \partial y)_{400}$ are estimated by a central-difference scheme of the first derivative and the CIRS thermal maps at 243- and 400-mbar pressure-levels. The estimation of β_z by this method is shown in the panel B of Fig. 12. In addition, the frequency N^2 in Eq. (3) is defined as $N^2 = g \partial \ln \theta / \partial z$, which we estimate using the CIRS average potential temperature θ at the two pressure-levels (243- and 400-mbar). The resulting ex-

pression is $N^2 = g/(0.5\bar{\theta}_{243} + 0.5\bar{\theta}_{400})[(\bar{\theta}_{243} - \bar{\theta}_{400})/\Delta z] = 3 \times 10^{-4} \text{ s}^{-2}$ for 315-mbar, which is consistent with the value in Voyager times (Achterberg and Ingersoll, 1989). The scale height $H = R\bar{T}/g$ is calculated to be $1.8 \times 10^4 \text{ m}$ at the 315-mbar by setting the \bar{T} as the average temperature of the 400- and 243-mbar pressure-levels. Fig. 12 (panel B) shows β_e within the latitude range $[5^\circ \text{ N}, 25^\circ \text{ N}]$.

Fig. 10 shows that the NEB wave appears in both CIRS 400- and 243-mbar maps without obvious phase shift. In addition, Figs. 2 and 3 suggest that the NEB wave penetrates down at least to the pressure level of the UV1 filter, which is around 0.5 bar (Li et al., 2006). Therefore, the half-wavelength of the NEB wave is larger than the altitude difference between the 243- and 500-mbar levels, which means that the vertical wavelength of the NEB wave is larger than 1 scale height.

In the WKB approximation, the meridionally trapped wave has to satisfy $\int_{y_1}^{y_2} l(y) dy = (n + 1/2)\pi$ (Morse and Feshbach, 1953, pp. 1099–1099), where y_1 and y_2 are the turning points—the meridional boundaries of the trapping region—the latitudes where $l^2 = 0$. Since the wave appears to have only a single maximum in latitude, the number n is set to 1 in our case although this violates the condition of the WKB method. Evaluating the meridional wave-number $l(y)$ with Eq. (3) for different values of the vertical wave-number m , we find that the condition $\int_{y_1}^{y_2} l(y) dy = (3/2)\pi$ is satisfied when $m = 0.39 \times 10^{-4} \text{ m}^{-1}$, corresponding to a vertical wave-length 160 km. This is around 9 scale heights at the 315-mbar level, which is at least consistent with the previous conclusion that the vertical wavelength of the NEB wave is larger than 1 scale height. We also tried larger values of the meridional mode number n ($n = 2, 3, 4, \dots$), but the condition $\int_{y_1}^{y_2} l(y) dy = (n + 1/2)\pi$ could only be satisfied with negative m^2 . The trapping latitude range in that case is larger than 30° (i.e., the lower turning point $y_1 < 0^\circ$ and the polar turning point $y_2 > 30^\circ \text{ N}$), which is inconsistent with the observational trapping latitude range $\sim 9^\circ$ ($y_1 \sim 10^\circ \text{ N}$ and $y_2 \sim 19^\circ \text{ N}$).

Fig. 13 shows l^2 as a function of latitude at the 315 mbar level, assuming m is constant with latitude and equal to $0.39 \times 10^{-4} \text{ m}^{-1}$, the value that satisfies $\int_{y_1}^{y_2} l(y) dy = (3/2)\pi$. In general, m could vary with latitude and altitude. In a full treatment using the WKB approximation, one would launch rays in various directions from various locations and compute m^2 and l^2 along the ray path. Such detailed calculations are not justified in our case, first because we have almost no information about m , and second because the WKB approximation is not valid for small m and l . Fig. 13 and the equation $\int_{y_1}^{y_2} l(y) dy = (3/2)\pi$ are useful only as a guide to show that trapping is possible within the latitude band centered around 14.5° N .

Fig. 13 shows that l^2 becomes negative when moving away from the latitude of the NEB wave (14.5° N): The wave is trapped within this range by reflections at the latitude boundaries (Salby, 1996, p. 465). The reversal of the sign of l^2 around 12.5 and 24° N is mainly due to the increasing eastward wind \bar{u} when moving away from the latitude of the NEB wave (14.5° N). This makes the term $\beta_e/(\bar{u} - c_x)$ in Eq. (3) very small and offers a possible trapping mechanism in the meridional direction. Fig. 13 suggests that the trapping is not complete at the

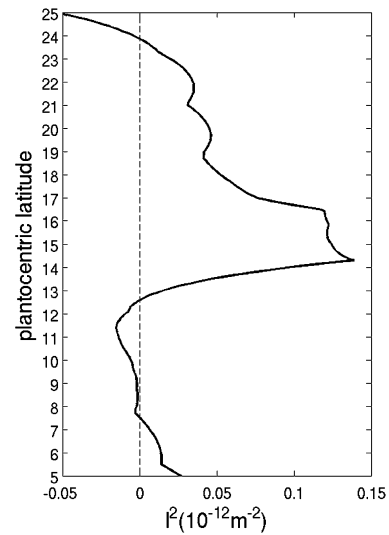


Fig. 13. The square of the meridional wave-number of the NEB wave. The calculation of the meridional wave-number l^2 is based on Eq. (3) and the values of β_e in Fig. 12. The vertical wave-length $L_z = 160 \text{ km}$ ($m = 0.39 \times 10^{-4} \text{ m}^{-1}$) is kept constant within the 315-mbar pressure surface in the above calculation.

lower latitude: Wave energy could leak out to the south, since the region of negative l^2 is neither deep nor wide.

Although the preceding analysis does imply qualitatively that the wave is trapped near 14.5° , the latitudes at which l^2 changes sign (12.5 and 24° N) do not agree quantitatively with the observed boundaries of the wave (10 and 19° N). In addition, uncertainties exist in the estimation of β_e and the vertical wave-number m . Detailed discussion of the propagation of the NEB wave has to involve a full wave analysis, but the theory will introduce more unknown parameters like the initial conditions. Such analysis is beyond the scope of this paper.

4.3. Vertical propagation of the NEB wave

When the zonal wind varies with height, the wave may encounter a *critical level*, which is defined as a level where $\bar{u} - c_x = 0$. The classical theory (Salby, 1996) says that $m \rightarrow \infty$ at the critical level and the wave is absorbed. Fig. 6 shows that the phase velocity of the NEB wave is smaller than the UV1 ambient flow at ~ 0.5 bar (Li et al., 2006) and larger than the corresponding CB2 ambient flow at ~ 0.7 bar (Banfield et al., 1998). Fig. 14 verifies this point again by comparing the phase velocity with the CIRS zonal winds at 315- and 499-mbar. These facts suggest that the phase velocity of the NEB wave will be equal to the ambient flow ($\bar{u} - c_x = 0$) somewhere between the pressure-level ~ 0.5 bar and the pressure-level ~ 0.7 bar. Therefore, the NEB wave will be absorbed between 0.5 and 0.7 bar when its perturbation energy propagates downward. This conclusion seems to support the second explanation for why the wave is not seen clearly in the other 7 filters of the ISS (Figs. 2 and 3)—it does not exist at the pressure-levels sampled by these filters. The vertical structure of the zonal winds from CIRS (Flasar et al., 2004a; Simon-Miller et al., 2006) shows that the wind at 14.5° N is westward relative to the wave at 0.7 bar (CB2), changes sign

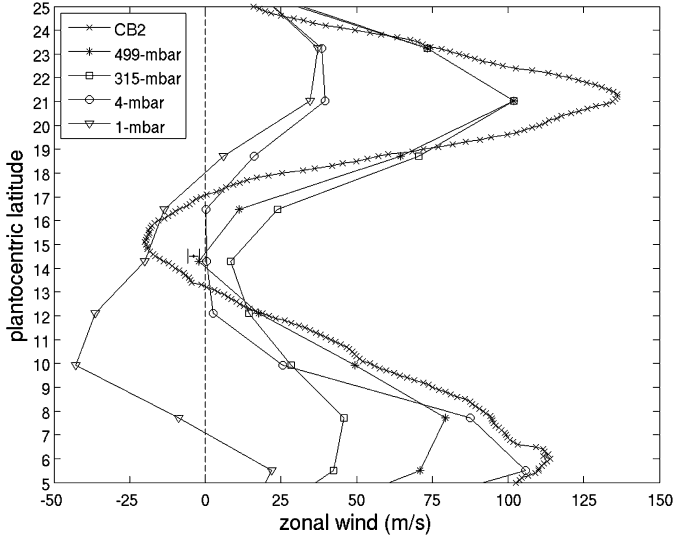


Fig. 14. CIRS zonal wind profiles at different pressure levels, phase velocity of the NEB wave, and CB2 zonal winds at the pressure level of visible cloud deck. The red dot with error-bar represents the phase velocity of the NEB wave. The CB2 zonal winds are same as the CB2 zonal winds used in Fig. 8, but more latitudes are included.

near 499-mbar, is eastward at 315-mbar, changes sign again near 4-mbar, and finally becomes westward at 1-mbar. This suggests that the NEB wave can propagate between the 499 and 4 mbar levels and will be absorbed around the pressure-level ~ 4 -mbar. The analysis is consistent with the CIRS observations that the NEB wave is seen in the 243- and 400-mbar temperature maps, but not seen in the 1- and 4-mbar temperature maps (Fig. 10).

4.4. Generating mechanism of the NEB wave

The property that the NEB wave is quasi-stationary relative to System III suggests that it is deep-rooted, although it cannot be seen in the continuum band images, which are sensitive to the deep jovian atmosphere. In addition, the NEB wave cannot propagate up from below through the critical level, since $\bar{u} - c_x = 0$ between the pressure-level ~ 0.5 bar and the pressure-level ~ 0.7 bar. Either the wave is generated between 0.5 bar and 4 mbar, or else it propagates in from the sides, having been generated below and to the north or south of 14.5° N latitude. Moist convective storms are always active in the 6 – 15° N cyclonic regions (Little et al., 1999; Porco et al., 2003). Some strong convective storms can penetrate to altitudes above the 0.5-bar level (Li et al., 2006). The dynamical disturbance and the corresponding heating associated with these convective storms could be a generating mechanism for the NEB wave if we assume it is generated between 0.5 bar and 4 mbar.

Likewise, the circumpolar wave at 48.5° S could not be seen in the continuum band images, which suggests that it is generated in the upper troposphere or stratosphere. Some long-lived vortices are located at the latitudes of the circumpolar wave. An example of such vortices is shown in the global MT3 and CB3 maps of Fig. 2 with location at 48.5° S, 355° W. Flow distur-

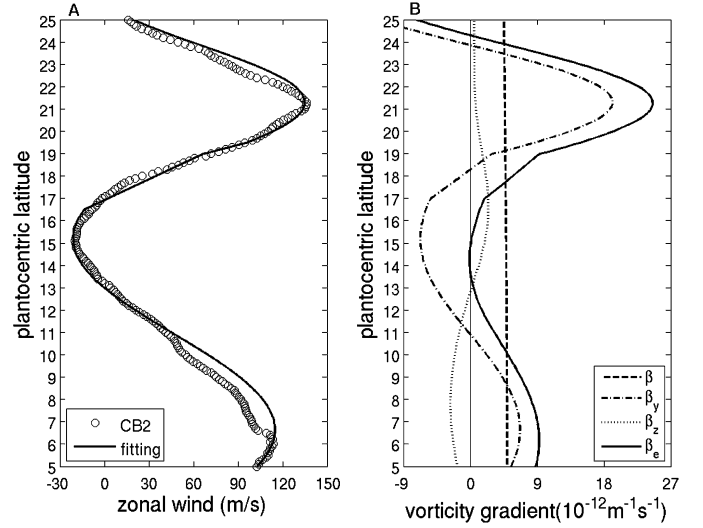


Fig. 15. CB2 zonal wind profile and meridional gradients of vorticity within the latitude range of the NEB wave at the visible cloud deck (~ 0.7 bar). (A) The CB2-mbar zonal wind profile around the latitude range of the NEB wave and a cosine function fit. (B) The vorticity gradients β , β_y , β_z , and β_e at ~ 0.7 bar. The β_y at 315 mbar is used for the CB2 pressure-level because the temperature fields at ~ 0.7 bar is unavailable.

bance above these vortices could create an obstacle in the flow that gives rise to the high-altitude circumpolar waves including the wave centered at 48.5° S. Furthermore, the upward momentum transportation associated with breaking or dissipation of small-scale gravity waves could be the origin of planetary waves in the upper atmosphere (Smith, 2003).

In general, Kelvin–Helmholtz (KH) instability due to strong wind shear can serve as a mechanism to generate atmospheric waves. Bosak and Ingersoll (2002) show that such instability can occur in the lower troposphere around 5–10 bar but not in the upper troposphere because the Richardson number is larger than 1.0 due to the large static stability there. In addition, Bosak and Ingersoll (2002) show that the waves due to KH instability have horizontal wavelength on the order of 300 km, which is several times the thickness of the shear layer. This is much smaller than the wavelengths of the NEB wave and the circumpolar wave in this study. Therefore, the KH instability can be ruled out as a generating mechanism for the two waves in this study.

The third possible generating mechanism is baroclinic instability. Achterberg and Flasar (1996) suggested that a changing potential vorticity gradient can be a source of planetary waves in Saturn's upper troposphere. Our estimation of the potential vorticity gradient (β_e in Fig. 12) shows that the gradient is always positive within the latitude range of the NEB wave at the 315-mbar pressure-level, which suggests that the ambient flows are stable at the 315-mbar pressure-level. However, there are uncertainties in our estimates of the potential vorticity gradient β_e as we discussed in Section 4.2. Here we assume that the deeper visible cloud deck (~ 0.7 bar) has the same value of β_z as the 315-mbar pressure-level and calculate the potential vorticity gradient β_e at the visible cloud deck based on the CB2 zonal wind measurements. The resulting β_e at the pressure-level of the visible cloud deck is shown in Fig. 15. Fig. 15 shows that

the potential vorticity gradient β_e is negative around the center of the NEB wave (latitude 14.5° N) at the visible cloud deck (~ 0.7 bar), which is the result of the increasing curvature of the eastward jets when going deeper. Therefore, the baroclinic instability could be a candidate of the source of the NEB wave.

5. Summary and discussion

One NEB wave and one circumpolar wave were observed in the ISS multi-filter images. Their properties (wavelength, period, and movement relative to the ambient flows) suggest that the two waves are planetary waves. The simultaneous comparison between the ISS and CIRS (Porco et al., 2003; Flasar et al., 2004a) confirms that the waves seen by the two instruments are the same. Furthermore, the combined observations from the ISS and CIRS offer a possible explanation of why the NEB wave is trapped in the vertical and meridional directions.

The near-simultaneous comparison between the ISS and CIRS observations connects the large dark oval in polar region in the UV1 images to the warm regions in the CIRS thermal maps. The large oval is dark in UV1 and warm in the CIRS, which suggests that it is composed of UV-absorbing particles transported down from above. In addition, the CIRS thermal maps suggest that the UV1 dark oval is located above the 4-mbar pressure surface.

Sanchez-Lavega et al. (1998) noticed that Jupiter's 67° S circumpolar waves (wavelength 15,000 km) and Saturn's hexagon at 79° N have an interesting relationship between the numbers n of wavelengths in the corresponding planetary circumference: $n(67^\circ \text{ S})/n(79^\circ \text{ N}) \approx \cos(67^\circ)/\cos(79^\circ)$. The circumpolar wave system centered at 48.5° S in this study and the 67° S wave discovered by Sanchez-Lavega et al. (1998) have the same relationship: $n(48.5^\circ \text{ S})/n(67^\circ \text{ S}) \approx \cos(48.5^\circ)/\cos(67^\circ)$. In other words, the two circumpolar waves on Jupiter have the same wavelength because the radius is proportional to cosine of the latitude. The two waves share other properties. Firstly, they are both quasi-stationary relative to the System III (phase velocity 4 m s^{-1} for the 48.5° S wave and 2 m s^{-1} for the 67° S wave). Secondly, the CIRS polar stratospheric zonal winds (Simon-Miller et al., 2006) based on the thermal wind equation and the CIRS thermal maps suggest that the 67° S circumpolar wave is embedded in the stratospheric eastward jets, which is same with the 48.5° S wave in this paper. As we discussed in Section 4.4, the negative β_y due to the eastward jets can change the sign of the potential vorticity gradient β_e , which offers a possible source not only for the NEB wave but also for the circumpolar waves.

Acknowledgment

This research was supported primarily by Cassini project funds.

References

Achterberg, R.K., Flasar, F.M., 1996. Planetary-scale thermal waves in Saturn's upper troposphere. *Icarus* 119, 350–369.

- Achterberg, R.K., Ingersoll, A.P., 1989. A normal-mode approach to jovian atmospheric dynamics. *J. Atmos. Sci.* 46, 2448–2462.
- Allison, M.D., 1990. Planetary waves in Jupiter's equatorial atmosphere. *Icarus* 83, 282–307.
- Banfield, D., Gierasch, P.J., Squyres, S.W., Nicholson, P.D., Conrath, B.J., Matthews, K., 1996. 2 μm spectrophotometry of jovian stratospheric aerosols—Scattering opacities, vertical distributions, and wind speeds. *Icarus* 121, 389–410.
- Banfield, D., Gierasch, P.J., Bell, M., Ustinov, E., Ingersoll, A.P., Vasavada, A.R., West, R.A., Belton, M.J.S., 1998. Jupiter's cloud structure from Galileo imaging data. *Icarus* 135, 230–250.
- Bosak, T., Ingersoll, A.P., 2002. Shear instabilities as a probe of Jupiter's atmosphere. *Icarus* 158, 401–409.
- Deming, D., Mumma, M.J., Espenak, F., Jennings, D.E., Kostiuik, T., Wiedemann, G., Loewenstein, R., Piscitelli, J., 1989. A search for p-mode oscillations of Jupiter—Serendipitous observations of nonacoustic thermal wave structure. *Astrophys. J.* 343, 456–467.
- Deming, D., Reuter, D., Jennings, D., Bjoraker, G., McCabe, G., Fast, K., Wiedemann, G., 1997. Observations and analysis of longitudinal thermal waves on Jupiter. *Icarus* 126, 301–312.
- Flasar, F.M., Gierasch, P.J., 1986. Mesoscale waves as a probe of Jupiter's deep atmosphere. *J. Atmos. Sci.* 43, 2683–2707.
- Flasar, F.M., Kunde, V.G., Achterberg, R.K., Conrath, B.J., Simon-Miller, A.A., Nixon, C.A., Gierasch, P.J., Romani, P.N., Bezaud, B., Irwin, P., Bjoraker, G.L., Brasunas, J.C., Jennings, D.E., Pearl, J.C., Smith, M.D., Orton, G.S., Spilker, L.J., Carlson, R., Calcutt, S.B., Read, P.L., Taylor, F.W., Parrish, P., Barucci, A., Courtin, R., Coustenis, A., Gautier, D., Lellouch, E., Marten, A., Prange, R., Biraud, Y., Fouchet, T., Ferrari, C., Owen, T.C., Abbas, M.M., Samuelson, R.E., Raulin, F., Ade, P., Cesarsky, C.J., Grossman, K.U., Coradini, A., 2004a. An intense stratospheric jet on Jupiter. *Nature* 427, 132–135.
- Flasar, F.M., and 45 colleagues, 2004b. Exploring the Saturn system in the thermal infrared: The Composite Infrared Spectrometer. *Space Sci. Rev.* 115, 169–297.
- French, R.G., Gierasch, P.J., 1974. Waves in the jovian upper atmosphere. *J. Atmos. Sci.* 31, 1707–1712.
- Godfrey, D.A., 1988. A hexagonal feature around Saturn's north pole. *Icarus* 76, 335–356.
- Hinson, D.P., Magalhaes, J.A., 1991. Equatorial waves in the stratosphere of Uranus. *Icarus* 94, 64–91.
- Hinson, D.P., Magalhaes, J.A., 1993. Inertio-gravity waves in the atmosphere of Neptune. *Icarus* 105, 142–161.
- Holton, J.R., 2004. Introduction to Dynamic Meteorology, fourth ed. Academic Press, San Diego.
- Hord, C.W., West, R.A., Simmons, K.E., Coffeen, D.L., Sato, M., Lane, A.L., Bergstralh, J.T., 1979. Photometric observations of Jupiter at 2400 angstroms. *Science* 206, 956–959.
- Li, L., Ingersoll, A.P., Vasavada, A.R., Simon-Miller, A.A., Del Genio, A.D., Ewald, S.P., Porco, C.C., West, R.A., 2006. Vertical wind shear on Jupiter from Cassini images. *J. Geophys. Res.* 111, doi:10.1029/2005JE002556.
- Little, B., Anger, C.D., Ingersoll, A.P., Vasavada, A.R., Senske, D.A., Breneman, H.H., Borucki, W.J., and the Galileo SSI Team, 1999. Galileo images of lightning on Jupiter. *Icarus* 142, 306–323.
- Magalhaes, J.A., Weir, A.L., Conrath, B.J., Gierasch, P.J., Leroy, S.S., 1989. Slowly moving thermal features on Jupiter. *Nature* 337, 444–447.
- Minnaert, M., 1941. The reciprocity principle in lunar photometry. *Astrophys. J.* 93, 403–410.
- Morse, P.M., Feshbach, H., 1953. Methods of Theoretical Physics. Part II. McGraw-Hill, New York.
- Ortiz, J.L., Orton, G.S., Friedson, A.J., Stewart, S.T., Fisher, B.M., Spencer, J.R., 1998. Evolution and persistence of 5- μm hot spots at the Galileo probe entry latitude. *J. Geophys. Res.* 103, 23051–23069.
- Orton, G.S., Friedson, A.J., Caldwell, J., Hammel, H.B., Baines, K.H., Bergstralh, J.T., Martin, T.Z., Malcolm, M.E., West, R.A., Golisch, W.F., Griep, D.M., Kaminski, C.D., Tokunaga, A.T., Baron, R., Shure, M., 1991. Thermal maps of Jupiter: Spatial organization and time dependence of stratospheric temperature, 1980 to 1990. *Science* 252, 537–542.
- Orton, G.S., and 18 colleagues, 1994. Spatial organization and time dependence of Jupiter's tropospheric temperatures, 1980–1993. *Science* 265, 625–631.

- Orton, G.S., and 16 colleagues, 1998. Characteristics of the Galileo probe entry site from Earth-based remote sensing observations. *J. Geophys. Res.* 103, 22791–22814.
- Porco, C.C., West, R.A., McEwen, A., Del Genio, A.D., Ingersoll, A.P., Thomas, P., Squyres, S., Dones, L., Murray, C.D., Johnson, T.V., Burns, J.A., Brahic, A., Neukum, G., Veverka, J., Barbara, J.M., Denk, T., Evans, M., Ferrier, J.J., Geissler, P., Helfenstein, P., Roatsch, T., Throop, H., Tiscareno, M., Vasavada, A.R., 2003. Cassini imaging of Jupiter's atmosphere, satellites, and rings. *Science* 299, 1541–1547.
- Porco, C.C., West, R.A., Squyres, S., McEwen, A., Thomas, P., Murray, C.D., Delgenio, A., Ingersoll, A.P., Johnson, T.V., Neukum, G., Veverka, J., Dones, L., Brahic, A., Burns, J.A., Haemmerle, V., Knowles, B., Dawson, D., Roatsch, T., Beurle, K., Owen, W., 2004. Cassini Imaging Science: Instrument characteristics and anticipated scientific investigations at Saturn. *Space Sci. Rev.* 115 (1–4), 363–497.
- Pryor, W.R., Hord, C.W., 1991. A study of photopolarimeter system UV absorption data on Jupiter, Saturn, and Neptune: Implications for auroral haze formation. *Icarus* 91, 161–172.
- Rages, K., Beebe, R., Senske, D., 1999. Jovian stratospheric hazes: The high phase angle view from Galileo. *Icarus* 139, 211–226.
- Salby, M.L., 1996. *Fundamentals of Atmospheric Dynamics*. Academic Press, San Diego.
- Sanchez-Lavega, A., Hueso, R., Acarreta, J.R., 1998. A system of circumpolar waves in Jupiter's stratosphere. *Geophys. Res. Lett.* 25, 4043–4046.
- Showman, A.P., Dowling, T.E., 2000. Nonlinear simulations of Jupiter's 5-micro hot spots. *Science* 289, 1737–1740.
- Simon-Miller, A.A., Banfield, D., Gierasch, P.J., 2001. An HST study of jovian chromophores. *Icarus* 149, 94–106.
- Simon-Miller, A.A., Conrath, B.J., Gierasch, P.J., Orton, G.S., Achterberg, R.K., Flasar, F.M., Fischer, B.M., 2006. Jupiter's atmospheric temperatures: From Voyager IRIS to Cassini CIRS. *Icarus* 180, 98–112.
- Smith, A.K., 2003. The origin of stationary planetary waves in the upper mesosphere. *J. Atmos. Sci.* 60, 3033–3041.
- Smith, B.A., and 22 colleagues, 1979a. Jupiter system through the eyes of Voyager-1. *Science* 204, 951–957, 960–972.
- Smith, B.A., and 21 colleagues, 1979b. Galilean satellites and Jupiter—Voyager-2 imaging science results. *Science* 206, 927–950.
- Tomasko, M.G., Karkoschka, E., Martinek, S., 1986. Observations of the limb darkening of Jupiter at ultraviolet wavelengths and constraints on the properties and distribution of stratospheric aerosols. *Icarus* 65, 128–243.
- Vincent, M.B., Clarke, J.T., Ballester, G.E., Harris, W.M., West, R.A., Trauger, J.T., Evans, R.W., Stapelfeldt, K.R., Crisp, D., Burrows, C.J., Gallagher, J.S., Griffiths, R.E., Hester, J., Hoessel, J.G., Holtzman, J.A., Mould, J.R., Scowen, P.A., Watson, A.M., Westphal, J.A., 2000. Jupiter's polar regions in the ultraviolet as imaged by HST/WFPC2: Auroral-aligned features and zonal motions. *Icarus* 143, 205–222.
- West, R.A., 1988. Voyager 2 imaging eclipse observations of the jovian high altitude haze. *Icarus* 75, 381–398.
- West, R.A., Baines, K.H., Friedson, A.J., Banfield, D., Ragent, B., Taylor, F.W., 2004. Jupiter: The planet, satellites and magnetosphere. In: Bagenal, F., Dowling, T.E., McKinnon, W.B., Jewitt, D., Murray, C., Bell, J., Lorenz, R., Nimmo, F. (Eds.), *Cambridge Planetary Science*. Cambridge Univ. Press, New York, p. 81.
- Young, L.A., Yelle, R.V., Young, R., Seiff, A., Kirk, D.B., 2005. Gravity waves in Jupiter's stratosphere, as measured by the Galileo ASI experiment. *Icarus* 173, 185–199.